Not so non-marine?
Revisiting the Stoer Group and the Mesoproterozoic biosphere

E.E. Stüeken[1,2,3]*, E.J. Bellefroid[4], A. Prave[1],
D. Asael[4], N.J. Planavsky[4], T.W. Lyons[2]

OPEN ACCESS

Abstract

The Poll a'Mhuilt Member of the Stoer Group (Torridonian Supergroup) in Scotland has been heralded as a rare window into the ecology of Mesoproterozoic terrestrial environments. Its unusually high molybdenum concentrations and large sulphur isotope fractionations have been used as evidence to suggest that lakes 1.2 billion years ago were better oxygenated and enriched in key nutrients relative to contemporaneous oceans, making them ideal habitats for the evolution of eukaryotes. Here we show with new Sr and Mo isotope data, supported by sedimentological evidence, that the depositional setting of this unit was likely connected to the ocean and that the elevated Mo and S contents can be explained by evapo-concentration of seawater. Thus, it remains unresolved if Mesoproterozoic lakes were important habitats for early eukaryotic life.

Introduction

Important steps in early biotic evolution may have occurred in lakes that offered distinct environmental conditions compared to the ocean. Support for this hypothesis has been reported from the Mesoproterozoic Poll a'Mhuilt Member (Stoer Group) in Scotland, which is interpreted as a fluvio-lacustrine deposit (Stewart, 2002). Parnell *et al.* (2010; 2015) documented large S isotope fractionations (up to 55 ‰) and Mo concentrations reaching 232 ppm that far exceed those of most contemporaneous marine shales. These features were interpreted as

1. School of Earth and Environmental Sciences, University of St. Andrews, St. Andrews, Fife, KY16 9AL, Scotland, UK
2. Department of Earth Sciences, University of California, Riverside CA 92521, USA
3. Virtual Planetary Laboratory, University of Washington, Seattle WA 98195, USA
* corresponding author (email: ees4@st-andrews.ac.uk)
4. Department of Geology and Geophysics, Yale University, New Haven CT 06520, USA

an indication that Mesoproterozoic lacustrine environments were more oxygenated and nutrient-rich than seawater, making them preferable habitats for eukaryotic organisms. However, the supposition that the Poll a'Mhuilt Member was deposited in a lacustrine setting rests on contestable lines of evidence: fluvial sandstones bracketing the proposed lacustrine interval and allegedly high boron concentrations in illite, which were regarded as ambiguous in the original study (Stewart and Parker, 1979; Stewart, 2002). Here we present new geochemical data and sedimentological features that indicate a marine influence, particularly during deposition of the Mo- and S-rich interval.

Geologic Setting

The mostly siliciclastic Stoer Group rests nonconformably on Archaean gneiss in northwest Scotland (Stewart, 1988). The depositional age is constrained to 1177 ± 5 Ma based on ^{40}Ar–^{39}Ar dating on diagenetic K-feldspar in the Stac Fada Member, an ancient impact deposit (Parnell *et al.*, 2011; Reddy *et al.*, 2015) immediately beneath the Poll a'Mhuilt Member (Fig. 1).
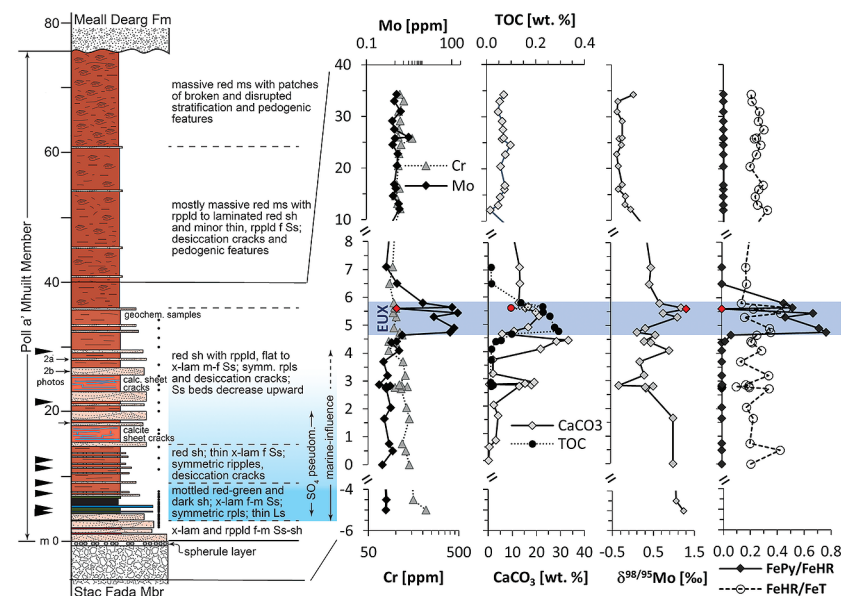

Figure 1   Stratigraphy of the Poll a'Mhuilt Member. EUX = euxinic interval. The horizon at 5.6 m (red symbols) was affected by modern oxidative weathering and is not considered in the discussion. Black arrows = locations of tidal indicators.

The basal ~3 m of the Poll a' Mhuilt Member consist of channeled, trough cross-bedded and planar laminated sandstone overlain by about 1–2 m of mottled grey-red shale with thin limestone beds followed up section by 2–4 m of calcareous dark grey shale. The limestone beds contain small-scale, chicken-wire fabric (calcite and albite pseudomorphs replacing gypsum). The carbonate is mostly micro-crystalline (Fig. S-1); secondary calcite replacements are minor. The next ~25 m consist of red shale and thin sandstone with abundant desiccation cracks and flat-laminated to ripple cross-laminated, 5–50 cm-thick beds of fine to medium sandstone which have abundant symmetrical (wave) ripples and locally developed herringbone cross-lamination (Fig. 2b), as well as flaser and lenticular bedding (Fig. 2a) and evaporite pseudomorphs after gypsum (Parnell *et al.*, 2010). The overlying (and major) part of the Poll a' Mhuilt Member (>~30 m) comprises massive red mudstone and flat-laminated to ripple cross-laminated fine sandstone and siltstone, all with desiccation cracks and pedogenic structures, such as disrupted and homogenised beds and pseudo-anticlines (Stewart, 2002).
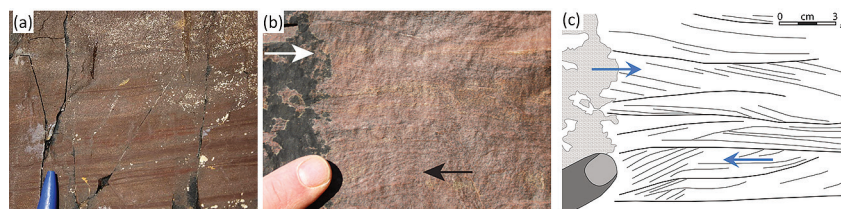

Figure 2 Sedimentary features compatible with a marine setting in the middle Poll a'Mhuilt Member. **(a)** Flaser- and lenticular-bedding. **(b)** Superposed sets of herringbone cross-lamination, 3D exposures confirm bi-directional character. Stratigraphic positions are marked in Figure 1. **(c)** Line drawing of sedimentary features showing superposed sets of bi-polar cross-laminated ripples (herringbone) with multiple reactivation surfaces commonly with thin clay drapes.

Methods

We collected outcrop samples extending from the upper 5 m of the Stac Fada Member through 35 m of the Poll a'Mhuilt Member, with emphasis on the calcareous grey shale (4.75 to 5.80 m, Fig. 1) (58.202422°N, 5.340425°W). Our analytical methods follow standard protocols as described in the Supplementary Information, with the exception of our carbonate-Sr extraction. As silicate phases can release Sr during acid-dissolution, we extracted carbonate-bound Sr with a ten-step sequential leaching procedure (modified after Liu *et al.*, 2013). This approach allowed us to construct a mixing curve between carbonate and silicate phases, where the latter can be monitored with Rb. The pure carbonate end-member was calculated by extrapolation to a Rb/Sr ratio of zero. Bedrock samples were analysed for Sr isotopes after bulk digestions and back-calculated to 1.2 Ga using measured Rb/Sr ratios and the $^{87}Sr \leftarrow ^{87}Rb$ decay constant to account for ^{87}Rb decay.

Results

Similar to Parnell *et al.* (2015), we found high Mo concentrations of up to 166 ppm in the grey shale of the Poll a'Mhuilt Member (4.75–5.80 m), which is 180 times higher than in the surrounding red shales (Fig. 1). Other transition metals show weak to no enrichments in the grey shale (Table S-3). Nickel and Cr are elevated in the volcanic/impact breccia of the Stac Fada Member and then decrease slowly into the Poll a'Mhuilt Member.

Ratios of highly reactive Fe (Fe_{HR}; bound in oxides, sulphides and carbonates) to total Fe (Fe_T) fall between 0.15 and 0.49 in the grey shale unit, while ratios of pyrite-bound Fe (Fe_{Py}) to Fe_{HR} range from 0.46 to 0.78 (Fig. 3a). Carbon to sulphur ratios range from 0.1 to 1.2 (median 0.2) in the grey shale. Molybdenum isotope data show positive values in the Stac Fada Member (+1.15 ‰), then progressively decrease in the first red shale (~0 m to 4 m), followed up section by an increase to a maximum of +1.19 ‰ in the grey shale (5.65 m, Fig. 1). In the overlying red shale (12 to 33 m), $\delta^{98}Mo$ drops to -0.38 ‰. Carbonate $\delta^{18}O$ and $\delta^{13}C$ values throughout the section covary (Fig. 3b). Carbonate-bound $^{87}Sr/^{86}Sr$ ratios in the red and grey shale (4.10–5.65 m) trend toward end-members of 0.707–0.710 (Fig. 3c). Two gneiss samples from the Lewisian basement, back-calculated to 1.2 Ga, have $^{87}Sr/^{86}Sr$ ratios of 0.721 ± 0.008; two amphibolite dyke samples and two Stac Fada samples average around 0.704 ± 0.002 and 0.706 ± 0.0004, respectively.
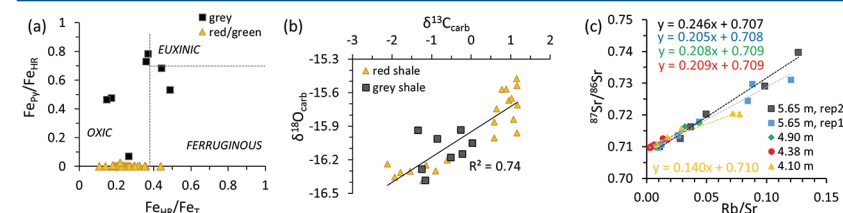

Figure 3 **(a)** Iron speciation, **(b)** carbonate C and O isotopes, and **(c)** carbonate-bound Sr isotopes. Dashed lines in (a) mark redox transitions (Poulton and Canfield, 2011). For comparison to our data in panel (b), values of contemporaneous unaltered marine carbonates fall between -10 ‰ and -7 ‰ for $\delta^{18}O_{carb}$ and 0 ‰ and +2 ‰ for $\delta^{13}C_{carb}$ (Shields and Veizer, 2002) (see Fig. S-2 for discussion). In panel (c), data points represent individual leaches increasing acid strength; y-axis intercept = carbonate end-member.

Discussion

Some sedimentary features in the Poll a'Mhuilt Member provide unequivocal evidence for a largely subaerial depositional setting: the basal (<3 m) channelised and trough cross-bedded sandstones and unimodal palaeocurrent indicators imply fluvial deposition (Stewart, 2002) and the abundant pedogenic features

in the upper part (30 m) of the member indicate deeply palaeo-weathered alluvium (Stewart, 2002). However, within the 3–30 m interval that contains the calcareous and grey shale we observed flaser, pin-stripe and lenticular bedding; multiple reactivation surfaces; mud drapes and herringbone cross-lamination (Fig. 1). These features are strong evidence of tidally influenced sedimentation on marine tidal flats (Davis Jr., 2012). Closely interfingered marine and non-marine deposition is not uncommon in the rock record. For example, recent discoveries of tidal indicators in the Ordovician Juniata Formation raised doubts about some of the oldest purported evidence for land colonisation by animal life (Davies *et al.*, 2010). Our sedimentological observations raise similar concerns for the eukaryotic biota of the Stoer Group (Cloud and Germs, 1971). This view is supported by our geochemical data, which are most parsimoniously explained by a marine influence during the deposition of the middle Poll a'Mhuilt Member (~3–30 m).

Carbonate-bound $^{87}Sr/^{86}Sr$ ratios capture the isotope composition of the water column in which the carbonate precipitated. As typical continental runoff is more radiogenic (^{87}Sr-enriched) than seawater, $^{87}Sr/^{86}Sr$ values can distinguish between marine and non-marine environments (Veizer *et al.*, 1990; Spencer and Patchett, 1997). However, infiltration of secondary fluids during early or late diagenesis typically increases carbonate $^{87}Sr/^{86}Sr$ ratios (Banner and Hanson, 1990). Covariation and low values of $\delta^{18}O_{carb}$ and $\delta^{13}C_{carb}$, as seen in our samples, may indicate some degree of alteration by continental fluids (Fig. 3c) (Shields and Veizer, 2002; Bartley and Kah, 2004). However, alteration almost always leads to more radiogenic carbonate $^{87}Sr/^{86}Sr$ ratios (Banner and Hanson, 1990). Diagenetic fluids were likely sourced from the surrounding land surface and should have reflected the composition of the Lewisian tonalite-trondjemite-granodiorite gneiss (0.740 ± 0.033; Lyon *et al.*, 1975; this study; and see Supplementary Information for discussion). Therefore, the $^{87}Sr/^{86}Sr$ ratio of our least radiogenic carbonate end-member (0.707, Fig. 3b), directly from within the sulphide- and Mo-rich interval (Parnell *et al.*, 2015), provides a maximum constraint for the primary $^{87}Sr/^{86}Sr$ ratio of the water body from which the carbonate precipitated. This value is too low to reflect exclusively continental runoff from the Lewisian basement (>0.715), which should dominate the signal in a lacustrine setting. Instead, this value is better explained by mixing between fluvial and marine waters. The latter have an estimated composition of 0.705–0.706 at 1.2 Ga (Kuznetsov *et al.*, 2014).

Repetitive influxes of seawater, followed by evaporation, would favour the precipitation of gypsum as recorded by pseudomorphs in the middle Poll a'Mhuilt Member (3–30 m, Fig. 1). As previously proposed (Parnell *et al.*, 2010, 2015), a combination of proxies—including large S isotope fractionations consistent with pyrite formation in the water column, high Mo/Re ratios and large amounts of pyrite despite low TOC contents (low C/S ratios)—suggest that the water column turned euxinic (sulphidic) during the evaporitic phase, perhaps as a result of salinity stratification and cut-off from seawater inflow. This pattern is supported by the Fe chemistry (see Supplementary Information for detailed discussion). Briefly, in the grey shale, Fe_{HR}/Fe_T ratios at the upper end of the detrital threshold (Raiswell and Canfield, 1998, also inferred from red shales in

our study) are consistent with some iron enrichment under anoxic conditions, and Fe_{Py}/Fe_{HR} ratios of up to 0.8 are consistent with euxinia (Poulton and Canfield, 2011). This interpretation is bolstered by the observed high Mo levels that are almost always associated with at least intermittent euxinia in the modern and ancient ocean (Scott and Lyons, 2012). The red shales lack Fe_{HR}/Fe_T enrichments (Fig. 3a), consistent with oxic deposition at water depths probably shallower than those for the grey shale (Stewart, 2002).

Although seawater probably had low Mo levels at this time (*e.g.*, 1–10 nM, Reinhard *et al.*, 2013), the presence of gypsum pseudomorphs implies that the water in this setting evaporated by a factor of up to 11 (assuming 100 % Mesoproterozoic seawater with modern levels of dissolved Ca^{2+} and ≤ 2–10 mM SO_4^{2-}; Kah *et al.*, 2004; Luo *et al.*, 2014), which could have locally raised dissolved Mo concentrations (perhaps to near-modern levels of 105 nM). Ensuing euxinia would have pulled this concentrated Mo reservoir into sediments. Repeated seawater incursions, evapo-concentration and euxinia could have acted like a Mo pump, sustaining these sedimentary Mo enrichments.

The Mo isotope data are consistent with a marine influence. The $\delta^{98}Mo$ of seawater can be effectively captured in sediments when dissolved sulphide levels in the water column are high (Neubert *et al.*, 2008). Processes that cause sedimentary archives to deviate from capturing dissolved $\delta^{98}Mo$ consistently favour the light isotopes (Siebert *et al.*, 2006). Our maximum value of +1.19 ‰ therefore provides a minimum constraint for the composition of dissolved Mo. This result agrees with previous estimates for seawater from mid-Proterozoic basins (+1.0 ‰ to +1.3 ‰, Kendall *et al.*, 2015). We discount a non-marine interpretation because such heavy $\delta^{98}Mo$ values are only known from catchments marked by weathering of pyrite- or sulphate-rich rock (Neubert *et al.*, 2011), which was not the case here. Further, although the Stac Fada Member is isotopically heavy (+1.15 ‰), it cannot be a major Mo source to the Poll a'Mhuilt Member because the up-section decline in Cr concentrations (Fig. 1) indicates a steady decrease in the proportion of material reworked from the Stac Fada into the Poll a'Mhuilt. Lighter $\delta^{98}Mo$ values in the remainder of the succession likely resulted from either partial Mo remobilisation under oxic conditions (Kowalski *et al.*, 2013) or adsorption of isotopically light MoO_4^{2-} onto Fe-oxides (Goldberg *et al.*, 2009).

Conclusion

The combined geochemical data and sedimentary features characterising the middle Poll a'Mhuilt Member are most parsimoniously interpreted as recording a marine influence on deposition, which calls into question previous inferences that purely non-marine lakes offered particularly favourable conditions for eukaryotic organisms in the Mesoproterozoic (Parnell *et al.*, 2010, 2015). A high bar should be set for arguments favouring non-marine settings in palaeobiological studies because such an assertion carries profound implications for physiological and

biochemical characteristics of early life, as well as for its evolutionary history in marine settings. In the light of our data, the importance of non-marine environments in the expansion of eukaryotic life remains unknown.

Acknowledgements

Editor: Liane G. Benning

Additional Information

Supplementary Information accompanies this letter at www.geochemicalper-spectivesletters.org/article1725

Reprints and permission information are available online at http://www.geochemicalperspectivesletters.org/copyright-and-permissions

Cite this letter as: Stüeken, E.E., Bellefroid, E.J., Prave, A., Asael, D., Planavsky, N.J., Lyons, T.W. (2017) Not so non-marine? Revisiting the Stoer Group and the Mesoproterozoic biosphere. *Geochem. Persp. Let.* 3, 221–229.

References

Banner, J.L., Hanson, G.N. (1990) Calculation of simultaneous isotopic and trace element variations during water-rock interaction with applications to carbonate diagenesis. *Geochimica et Cosmochimica Acta* 54, 3123–3137.

Bartley, J.K., Kah, L.C. (2004) Marine carbon reservoir, C_{org}-C_{carb} coupling, and the evolution of the Proterozoic carbon cycle. *Geology* 32, 129–132.

Cloud, P., Germs, A. (1971) New pre-paleozoic nannofossils from the Stoer formation (Torridonian), Northwest Scotland. *Geological Society of America Bulletin* 82, 3469–3474.

Davies, N.S., Rygel, M.C., Gibling, M.R. (2010) Marine influence in the Upper Ordovician Juniata Formation (Potters Mills, Pennsylvania): implications for the history of life on land. *Palaios* 25, 527–539.

Davis Jr., R.A. (2012) Tidal signatures and their preservation potential in stratigraphic sequences. In: Davis Jr., R.A., Dalrymple, R.W.(Eds.) *Principles of Tidal Sedimentology.* Springer, Netherlands, 35–55.

Goldberg, T., Archer, C., Vance, D., Poulton, S.W. (2009) Mo isotope fractionation during adsorption to Fe (oxyhydr) oxides. *Geochimica et Cosmochimica Acta* 73, 6502–6516.

Kah, L.C., Lyons, T.W., Frank, T.D. (2004) Low marine sulphate and protracted oxygenation of the Proterozoic biosphere. *Nature* 431, 834–838.

Kendall, B., Komiya, T., Lyons, T.W., Bates, S.M., Gordon, G.W., Romaniello, S.J., Jiang, G., Creaser, R.A., Xiao, S., McFadden, K., Sawaki, Y., Tahata, M., Shu, D., Han, J., Li, Y., Chu, X., Anbar, A.D. (2015) Uranium and molybdenum isotope evidence for an episode of widespread ocean oxygenation during the late Ediacaran Period. *Geochimica et Cosmochimica Acta* 156, 173–193.

Kowalski, N., Dellwig, O., Beck, M., Gräwe, U., Neubert, N., Nägler, T.F., Badewien, T.H., Brumsack, H.J., van Beusekom, J.E., Böttcher, M.E. (2013) Pelagic molybdenum concentration anomalies and the impact of sediment resuspension on the molybdenum budget in two tidal systems of the North Sea. *Geochimica et Cosmochimica Acta* 119, 198–211.

Kuznetsov, A.B., Semikhatov, M.A., Gorokhov, I.M. (2014) The Sr isotope chemostratigraphy as a tool for solving stratigraphic problems of the Upper Proterozoic (Riphean and Vendian). *Stratigraphy and Geological Correlation* 22, 553–575.

Liu, C., Wang, Z., Raub, T.D. (2013) Geochemical constraints on the origin of Marinoan cap dolostones from Nuccaleena Formation, South Australia. *Chemical Geology* 351, 95–104.

Luo, G., Ono, S., Huang, J., Algeo, T.J., Li, C., Zhou, L., Robinson, A., Lyons, T.W., Xie, S. (2014) Decline in oceanic sulfate levels during the early Mesoproterozoic. *Precambrian Research,* 258, 36-47.

Lyon, T.D.B., Gillen, C., Bowes, D.R. (1975) Rb-Sr isotopic studies near the major Precambrian junction, between Scourie and Loch Laxford, northwest Scotland. *Scottish Journal of Geology* 11, 333–337.

Neubert, N., Heri, A.R., Voegelin, A.R., Nägler, T.F., Schlunegger, F., Villa, I.M. (2011) The molybdenum isotopic composition in river water: constraints from small catchments. *Earth and Planetary Science Letters* 304, 180–190.

Neubert, N., Nägler, T.F., Böttcher, M.E. (2008) Sulfidity controls molybdenum isotope fractionation into euxinic sediments: Evidence from the modern Black Sea. *Geology* 36, 775–778.

Parnell, J., Boyce, A.J., Mark, D., Bowden, S., Spinks, S. (2010) Early oxygenation of the terrestrial environment during the Mesoproterozoic. *Nature* 468, 290–293.

Parnell, J., Mark, D., Fallick, A.E., Boyce, A., Thackrey, S. (2011) The age of the Mesoproterozoic Stoer Group sedimentary and impact deposits, NW Scotland. *Journal of the Geological Society* 168, 349–358.

Parnell, J., Spinks, S., Andrews, S., Thayalan, W., Bowden, S. (2015) High Molybdenum availability for evolution in a Mesoproterozoic lacustrine environment. *Nature Communications* 6, doi:10.1038/ncomms7996.

Poulton, S.W., Canfield, D.E. (2011) Ferruginous conditions: a dominant feature of the ocean through Earth's history. *Elements* 7, 107–112.

Raiswell, R., Canfield, D.E. (1998) Sources of iron for pyrite formation in marine sediments. *American Journal of Science* 298, 219–245.

Reddy, S.M., Johnson, T.E., Fischer, S., Rickard, W.D.A., Taylor, R.J.M. (2015) Precambrian reidite discovered in shocked zircon from the Stac Fada impactite, Scotland. *Geology* 43, 899–902.

Reinhard, C.T., Planavsky, N.J., Robbins, L.J., Partin, C.A., Gill, B.C., Lalonde, S.V., Bekker, A., Konhauser, K.O., Lyons, T.W. (2013) Proterozoic ocean redox and biogeochemical stasis. *Proceedings of the National Academy of Sciences,* 110, 5357–5362.

Scott, C., Lyons, T.W. (2012) Contrasting molybdenum cycling and isotopic properties in euxinic versus non-euxinic sediments and sedimentary rocks: refining the paleoproxies. *Chemical Geology* 324, 19–27.

Shields, G., Veizer, J. (2002) Precambrian marine carbonate isotope database: Version 1.1. *Geochemistry Geophysics Geosystems* 3, doi: 10.1029/2001GC000266.

SIEBERT, C., MCMANUS, J., BICE, A., POULSON, R., BERELSON, W.M. (2006) Molybdenum isotope signatures in continental margin marine sediments. *Earth and Planetary Science Letters* 241, 723–733.

SPENCER, J.E., PATCHETT, P.J. (1997) Sr isotope evidence for a lacustrine origin for the upper Miocene to Pliocene Bouse Formation, lower Colorado River trough, and implications for timing of Colorado Plateau uplift. *Geological Society of America Bulletin* 109, 767–778.

STEWART, A.D. (1988) The Stoer Group, Scotland. In: Winchester, J.A. (Ed.) *Later Proterozoic stratigraphy of the North Atlantic regions.* Blackie, Glasgow, 97–103.

STEWART, A.D. (2002) *The later Proterozoic Torridonian rocks of Scotland: Their sedimentology, geochemistry and origin.* Geological Society, Bath, UK.

STEWART, A.D., PARKER, A. (1979) Palaeosalinity and environmental interpretation of red beds from the late Precambrian ('Torridonian') of Scotland. *Sedimentary Geology* 22, 229–241.

VEIZER, J., CLAYTON, R.N., HINTON, R.W., VON BRUNN, V., MASON, T.R., BUCK, S.G., HOEFS, J. (1990) Geochemistry of Precambrian carbonates: 3-shelf seas and non-marine environments of the Archean. *Geochimica et Cosmochimica Acta* 54, 2717–2729.

Not so non-marine? Revisiting the Stoer Group and the Mesoproterozoic biosphere

E.E. Stüeken[1,2,3]*, E.J. Bellefroid[4], A. Prave[1], D. Asael[4], N.J. Planavsky[4], T.W. Lyons[2]

Supplementary Information

The Supplementary Information includes:

➢ S1. Analytical Methods

➢ S2. Preservation of Primary Signatures

➢ S3. Potential Caveats for the Iron Redox Proxy

➢ Supplementary Information References

➢ Figures S-1 to S-2

➢ Tables S-1 to S-8

S1. Analytical Methods

1.1 Rock preparation

Samples were cut with a rock saw to remove weathered surfaces and then hammered into cm-sized chips. The chips were transferred into acid-washed glass beakers, cleaned twice with 2 N HCl (trace metal grade) for 10–15 seconds, and washed thoroughly with 18 MΩ DI-H_2O. The clean chips were air-dried for two days with light cover, and finally pulverised in a ball mill. Powders were stored in acid-washed scintillation vials.

1. School of Earth and Environmental Sciences, University of St. Andrews, St. Andrews, Fife, KY16 9AL, Scotland, UK
2. Department of Earth Sciences, University of California, Riverside CA 92521, USA
3. Virtual Planetary Laboratory, University of Washington, Seattle WA 98195, USA
* corresponding author (email: ees4@st-andrews.ac.uk)
4. Department of Geology and Geophysics, Yale University, New Haven CT 06520, USA

1.2 Organic carbon analyses

Organic carbon and carbonate carbon and oxygen isotopes were analysed at the University of Washington, following established techniques (*e.g.,* Stüeken, 2013). For organic carbon isotopes and total organic carbon (TOC) content, powders were first decarbonated with 6 N HCl (reagent grade) at 80 °C for three days. The decarbonated powders were washed three times with 18 MΩ DI-H$_2$O and then dried in a closed oven and finally transferred into muffled scintillation vials. For the analyses, powders were weighed into tin capsules and analysed by flash combustion with an elemental analyser (Costech) coupled to a continuous flow IR-MS (Thermo MAT253). Results (Table S-1) are expressed relative to VPDB for $\delta^{13}C_{org}$. Average reproducibility of replicate samples (1 standard deviation, SD) was 0.18 ‰ ($\delta^{13}C_{org}$) and average accuracy, as determined with calibrated in-house standards, was -0.04 ‰. The peak area was calibrated for carbon quantities with an average relative error of 2.5 %.

Table S-1 Organic carbon isotopes and abundances. TOC = total organic carbon, RE = relative error, SD = standard deviation.

position	TOC	RE	$\delta^{13}C_{org}$	SD
[m]	[%]	[%]	[‰]	[‰]
2.73	0.01	4.73	-27.22	1.14
2.77	0.02	4.62	-26.48	0.28
2.83	0.01	2.46	-26.80	0.23
2.87	0.01	0.21	-25.98	0.62
3.7	0.01	15.62	-28.11	0.84
4.1	0.02	2.71	-28.68	0.00
4.38	0.04	1.44	-28.85	0.12
4.42	0.07	2.61	-29.73	0.05
4.65	0.12	0.33	-30.96	0.07
4.75	0.36	1.02	-31.23	0.08
4.9	0.34	0.44	-30.86	0.01
5.3	0.32	1.10	-30.50	0.01
5.45	0.28	0.51	-30.38	0.01
5.6	0.12	0.79	-29.94	0.05
5.65	0.28	0.36	-30.29	0.05
5.8	0.17	1.70	-30.33	0.04
6.5	0.02	0.06	-26.27	0.46
7.1	0.01	5.30	-25.04	0.14

1.3 Inorganic carbon and oxygen isotopes

For carbonate analyses, untreated powders were weighed into glass vials, reacted with phosphoric acid at 80 °C for 10 minutes in a Kiel III Carbonate Device, and analysed with a dual-inlet IR-MS (Thermo Finnigan Delta Plus) (Stüeken, 2013). For oxygen isotopes, the mineralogy was assumed to be calcite based on staining

pink with alizarin red and reacting strongly with 2 M HCl. The calcite mineralogy is confirmed by Ca/Mg ratios mostly >10 measured in acetic acid extracts (see below). Results (Table S-2, Fig. S-2) are expressed relative to VPDP for both $\delta^{18}O_{carb}$ and $\delta^{13}C_{carb}$. Average reproducibility (1 SD of replicate sample analyses) was 0.02 ‰ for $\delta^{18}O_{carb}$ and 0.01 ‰ for $\delta^{13}C_{carb}$, and average accuracy, as determined with calibrated in-house standards was <-0.01 ‰ and -0.01 ‰. The CO$_2$ pressure in the mass spectrometer was calibrated for carbonate quantity with an average relative error of 2.7 %. Stratigraphic patterns in the $\delta^{18}O_{carb}$ and $\delta^{13}C_{carb}$ data are further discussed in Figure S-2. Although the $\delta^{18}O_{carb}$ data have probably been altered to lower values (see Shields and Veizer, 2002; Bartley and Kah, 2004 for comparison), an overall trend is preserved that shows the heaviest values in the most evaporitic facies, as expected from evaporitic enrichment (Fig. S-2).

Table S-2 Carbonate carbon and oxygen isotopes and carbonate abundances (carb.). SD = standard deviation, carb = carbonate content by weight, RE = relative error.

| position [m]	$\delta^{13}C_{carb}$ [‰]	SD [‰]	$\delta^{18}O_{carb}$ [‰]	SD [‰]	% carb.	RE [‰]
2.73	-1.94	0.01	-16.36	0.03	12.8	0.9
2.77	-1.78	0.00	-16.31	0.02	18.0	2.8
2.83	-1.54	0.01	-16.30	0.00	15.3	5.5
2.87	-1.22	0.04	-16.39	0.02	19.0	0.3
4.10	-1.14	0.01	-16.25	0.01	21.8	0.8
4.38	-0.90	0.00	-16.30	0.00	28.3	3.8
4.42	-0.61	0.01	-16.20	0.02	33.3	5.1
4.65	-1.35	0.00	-15.94	0.00	5.7	2.6
4.75	-1.25	0.01	-16.28	0.01	10.6	2.2
4.90	-1.16	0.00	-16.38	0.03	16.6	8.4
5.30	-0.23	0.00	-16.15	0.00	21.0	1.5
5.45	0.02	0.01	-16.05	0.05	19.7	0.0
5.60	-0.52	0.00	-16.18	0.03	15.4	0.5
5.65	-0.27	0.01	-15.93	0.01	16.6	0.4
5.80	-0.86	0.01	-16.01	0.03	12.6	0.7
6.50	-2.02	0.01	-15.06	0.02	13.2	0.5
7.10	-2.12	0.01	-16.24	0.02	13.0	6.2
16.05	0.58	0.01	-15.86	0.01	7.3	7.2
16.85	0.65		-15.75		7.5	
20.45	0.58		-16.00		5.7	
22.75	0.77		-15.57		7.7	
24.55	0.88	0.02	-15.57	0.02	9.7	0.2
25.75	0.96		-15.67		6.4	
25.95	1.03		-15.65		7.0	
27.55	1.07		-15.84		6.6	
29.15	1.15	0.00	-15.47	0.02	6.3	7.0
30.95	1.16		-15.71		4.7	
32.95	1.16		-15.54		5.4	
34.25	1.16	0.02	-15.96	0.03	6.9	0.1
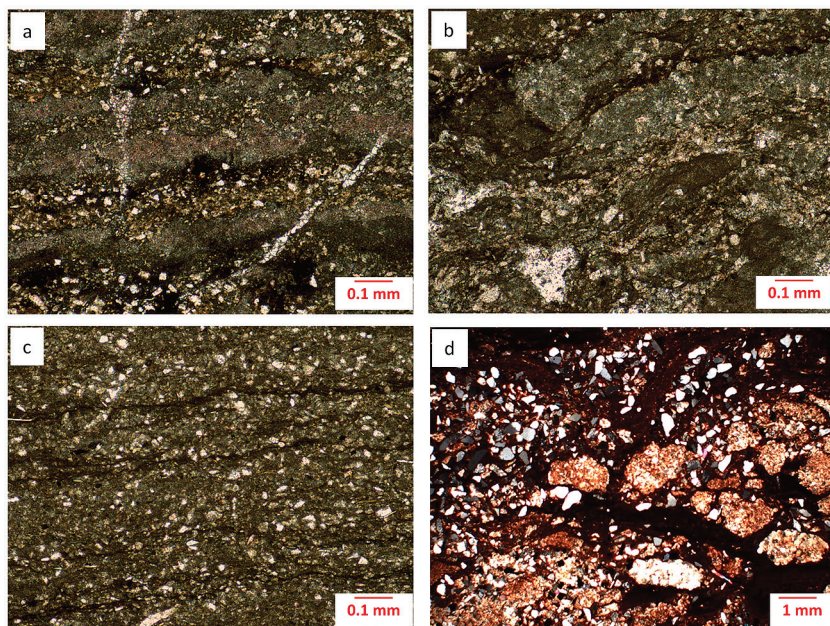
Figure S-1 Photomicrographs of the Poll a'Mhuilt Member. **(a)** Sample +2.77 m, plane-polarised light; calcareous red shale with 18 % CaCO₃ present as microcrystalline laminae, separated by iron-oxide coated siliciclastics. **(b)** Sample +4.42 m, plane-polarised light; calcareous red shale with 33 % CaCO₃ present as disrupted microcrystalline laminae and rare sparry fenestral fillings. **(c)** Sample +5.30 m, plane-polarised light; calcareous grey shale with 21 % CaCO₃ present as microcrystalline laminae, separated by kerogenous siliciclastics. **(d)** Sample +25.75 m, crossed polars; partially desiccated facies with 6 % CaCO₃ present as microcrystalline nodules and cement, stained with iron oxide, separated by iron-oxide coated siliciclastics. All samples contain angular silt grains composed of quartz, plagioclase, and K-feldspar and minor mica.

1.4 Bulk elemental abundances

Bulk digests were prepared at UC Riverside, following a method adapted from Reinhard *et al.* (2013a). Powders were first ashed at 800 °C in acid-washed ceramic crucibles, weighed before and after to determine the loss on ignition (LOI). Ashed powders were transferred into screw-top Teflon beakers and dissolved with 5ml HNO₃ + 1ml HF at 130 °C overnight. The acids were evaporated at 110–130 °C. Fluoride precipitates were removed through 1–2 treatments with aqua regia (3ml HCl + 1ml HNO₃) at 120 °C. Samples were stored in 5 % (v/v) HNO₃. All acids were trace metal grade and used in concentrated form.
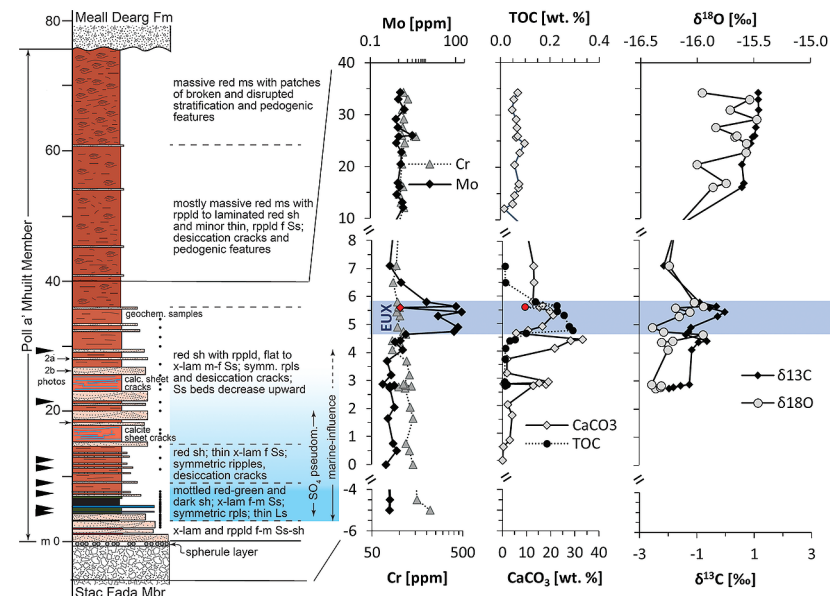

Figure S-2 Stratigraphic section through the Poll a'Mhuilt Member with carbonate C and O isotopes. Lithostratigraphy, Mo, Cr, CaCO₃ and TOC abundances are as in Figure 1 in the main text. The last panel shows δ¹⁸O and δ¹³C in carbonate in stratigraphic context. The trend highlights that the heaviest values in both isotopic proxies occur in the upper red shale. This is consistent with the high abundance of desiccation cracks in this part of the section, because evaporation forces these parameters to heavier values. The grey shale, which would have been most continuously flooded, shows relatively light values, consistent with a relatively lesser impact of evaporation. Despite the high degree of evaporation that is implied by the presence of gypsum pseudomorphs in the section (Stewart, 2002; Parnell *et al.*, 2010) the δ¹⁸O values are overall light compared to other mid-Proterozoic carbonates of similar age (Shields and Veizer, 2002; Bartley and Kah, 2004), which we attribute to fluid alteration. Oxygen isotopes are much more easily reset than carbon isotopes. However, the overall trend towards heavier values in the most evaporitic part of the section is preserved.

Elemental concentrations (Table S-3) were measured by ICP-MS (Agilent 7500ce). Reproducibility of replicate samples was 5 % on average. For Mo, which showed the largest range of concentrations, reproducibility was 20 % below 2 ppm and 4 % or better above 10 ppm. Accuracy was monitored with the USGS rocks standard SCo-1 and was within 5 % for minor elements and within 10 % for major elements.

Table S-3 Bulk elemental abundances. The grey shale unit extends from +4.75 m to +5.8 m; the sample from +5.6 m is likely altered by modern weathering. Samples below 0 m are from the Stac Fada Member and contain volcanic fragments. Abundances are in weight-percent or parts per million (µg/g).

position [m]	Na [%]	Mg [%]	Al [%]	P [%]	K [%]	Ca [%]	Ti [%]	V [ppm]	Cr [ppm]	Mn [ppm]	Fe [%]	Co [ppm]	Ni [ppm]	Cu [ppm]	Zn [ppm]	As [ppm]	Sr [ppm]	Mo [ppm]	Cd [ppm]	Pb [ppm]	Th [ppm]	U [ppm]
Poll a'Mhuilt section:																						
-5.00	3.36	2.23	6.78	0.07	1.80	0.46	0.37	72.3	217.3	712.9	4.43	29.8	400.6	9.8	78.6	2.4	170.0	0.4	0.0	9.6	4.1	0.7
-4.50	3.32	2.37	7.32	0.07	1.51	0.61	0.38	70.0	156.7	774.7	3.88	25.3	270.8	10.7	70.1	1.6	202.2	0.4	0.0	7.3	3.4	0.7
0.00	3.03	2.55	8.18	0.07	1.97	0.83	0.49	89.9	139.9	694.7	5.36	24.6	178.8	12.5	96.6	5.5	133.1	0.3	0.0	11.6	6.3	1.2
0.50	3.98	1.86	6.40	0.08	1.40	0.94	0.48	97.9	128.0	654.5	4.01	25.4	170.8	16.1	73.7	3.9	136.6	0.8	0.0	9.1	5.4	1.4
0.75	3.59	1.88	7.66	0.05	1.51	1.45	0.36	66.1	117.5	625.7	3.87	18.8	136.4	16.1	69.9	3.6	109.1	0.6	0.0	9.0	4.8	1.2
1.65	4.45	1.33	6.92	0.08	0.93	1.89	0.39	82.3	139.8	540.9	3.48	17.5	170.3	16.1	47.5	4.5	107.3	0.4	0.0	7.4	4.2	0.7
2.05	2.98	1.60	6.34	0.10	1.98	1.04	0.46	95.2	130.6	529.0	5.45	23.7	165.7	16.1	88.8	6.5	87.7	0.7	0.0	9.1	6.2	2.2
2.73	4.22	1.86	8.83	0.08	1.01	5.63	0.48	114.2	114.4	1025.6	3.70	21.1	94.3	16.1	63.6	4.2	116.1	0.5	0.0	14.4	5.5	5.2
2.77	3.32	1.41	7.22	0.07	1.15	7.49	0.43	87.9	98.2	1062.4	2.93	18.2	84.8	16.1	52.7	2.8	107.3	0.4	0.1	24.2	5.0	3.8
2.80	1.78	3.27	8.74	0.10	2.77	0.58	0.56	115.9	134.2	663.1	5.87	39.5	197.5	16.1	103.9	5.5	76.1	0.5	0.0	24.2	8.1	3.2
2.83	2.61	1.87	7.21	0.09	1.67	5.80	0.54	96.5	116.0	1125.6	3.84	27.4	129.6	16.1	78.4	4.3	101.1	0.6	0.1	19.4	5.5	4.7
2.87	3.12	1.78	7.19	0.07	1.38	7.58	0.43	89.4	110.0	1142.6	3.23	22.7	128.0	16.1	64.2	2.3	111.7	0.2	0.0	11.7	5.5	3.8
3.20	2.44	2.35	7.80	0.08	1.48	1.33	0.45	87.8	127.7	554.1	5.15	18.6	140.6	16.1	61.1	2.6	116.5	0.5	0.0	9.6	6.5	1.5
3.70	2.69	2.08	7.39	0.07	1.92	1.09	0.46	82.2	119.6	589.7	4.57	15.8	136.8	16.1	76.4	1.7	277.3	0.4	0.0	6.4	5.8	1.6
4.10	2.74	0.95	5.99	0.05	1.52	6.95	0.28	80.0	83.9	960.9	2.73	10.8	86.1	16.1	45.1	4.6	107.1	1.3	0.0	15.0	4.4	4.9
4.38	2.62	1.07	5.34	0.07	0.69	10.69	0.32	100.8	100.4	1171.7	2.95	16.9	99.6	16.1	48.7	3.1	142.5	0.7	0.1	13.8	4.6	4.7
4.42	2.42	0.85	4.60	0.07	0.70	12.84	0.32	82.3	83.6	1176.7	2.14	12.9	78.5	16.1	35.7	3.8	161.9	1.1	0.1	12.0	4.1	5.8
4.65	2.49	2.05	6.88	0.11	1.62	2.36	0.53	150.9	117.5	622.5	3.59	12.1	127.0	16.1	74.1	2.3	119.2	1.7	0.0	9.9	6.7	7.7
4.75	3.06	1.81	6.74	0.09	1.26	4.15	0.45	174.3	110.3	824.3	4.27	26.0	106.1	16.1	88.0	18.5	110.2	89.2	0.3	32.7	6.4	8.5
4.90	2.84	1.75	6.39	0.08	1.01	5.85	0.43	153.4	95.2	925.0	4.41	36.1	100.9	16.1	97.0	15.7	168.4	122.2	0.4	24.8	5.9	7.1
5.30	2.67	1.56	5.79	0.08	1.24	7.78	0.41	138.2	100.8	962.7	3.27	15.3	98.0	16.1	197.9	3.4	163.8	23.5	0.9	5.4	6.0	5.5
5.45	2.52	1.87	6.53	0.07	1.08	7.37	0.39	121.6	93.6	1205.2	4.48	20.6	110.2	16.1	137.1	27.9	94.4	166.2	1.8	50.6	5.8	3.8
5.60	2.39	1.87	8.71	0.09	2.19	5.73	0.46	119.1	100.1	880.1	4.48	19.0	105.0	16.1	150.9	2.2	154.3	1.1	0.3	4.9	6.1	3.4
5.65	2.78	1.72	6.07	0.08	1.28	6.19	0.46	119.1	97.6	1128.9	4.29	21.6	100.5	16.1	110.6	26.1	83.4	106.1	7.4	67.8	6.2	4.3
5.80	2.34	2.02	6.96	0.08	1.58	5.04	0.40	125.4	95.5	882.5	3.47	23.3	85.6	16.1	79.5	11.0	142.8	9.3	0.2	13.2	6.3	3.7
6.50	1.65	2.30	6.84	0.06	2.21	5.14	0.48	76.6	85.2	1056.2	4.12	15.1	75.7	16.1	99.5	0.2	147.0	1.1	0.1	4.0	7.0	1.9
7.10	2.65	1.77	6.79	0.06	1.38	5.18	0.41	69.9	92.4	919.3	4.05	13.3	62.5	16.1	67.7	2.5	87.3	0.4	0.0	5.7	5.7	1.4
12.10	1.49	2.92	8.46	0.09	3.29	0.80	0.57	157.0	114.3	583.1	5.83	23.9	101.6	16.1	99.9	25.5	66.4	1.4	-0.0	16.3	12.2	4.0
13.05	1.14	3.17	8.77	0.06	3.83	1.90	0.41	110.6	106.9	702.2	6.34	24.6	102.1	16.1	99.7	15.6	52.4	1.3	0.1	17.3	10.5	3.3
14.65	1.36	2.35	7.16	0.08	3.02	2.33	0.47	121.7	101.0	778.9	5.58	23.4	98.8	16.1	91.7	10.1	69.6	0.9	0.0	15.4	10.8	3.3
16.05	1.82	2.35	7.24	0.09	3.07	2.99	0.45	123.5	111.9	794.7	5.40	22.9	103.5	16.1	86.4	13.2	100.2	1.1	0.1	15.5	9.6	3.1
16.85	1.46	2.37	6.88	0.09	2.97	3.12	0.51	114.4	104.0	824.5	5.34	22.2	99.5	16.1	89.5	9.2	93.3	0.9	0.1	15.0	9.3	3.0
20.45	1.82	2.44	6.89	0.09	2.88	2.65	0.54	111.5	108.3	685.4	5.66	23.1	107.2	16.1	81.6	8.7	98.8	1.2	0.1	14.3	8.7	2.7
22.75	1.55	2.77	8.57	0.09	3.05	3.17	0.48	111.7	110.5	787.1	5.24	23.0	102.3	16.1	98.6	7.6	95.5	1.2	0.1	14.1	8.4	2.7
24.55	1.75	2.13	6.52	0.09	2.73	4.22	0.46	110.4	116.4	922.8	5.08	22.3	103.8	16.1	82.3	9.7	99.8	0.8	0.1	13.9	8.6	2.7
25.75	1.39	2.69	8.09	0.08	3.14	2.78	0.40	121.8	152.9	773.1	5.32	24.1	111.6	16.1	88.8	12.7	92.3	1.0	0.0	15.0	8.5	2.7
25.95	1.59	2.25	7.19	0.08	2.91	3.06	0.39	108.4	108.3	765.4	5.33	23.0	103.5	16.1	87.6	8.8	103.6	3.0	0.1	14.7	8.6	2.7
27.55	1.47	2.43	7.65	0.09	2.57	3.02	0.47	121.5	111.0	747.7	4.69	23.2	108.0	16.1	85.6	7.8	111.8	0.9	0.1	14.4	8.1	2.5
29.15	1.43	2.33	7.80	0.11	3.02	2.79	0.48	106.8	113.5	702.0	5.14	21.5	102.5	16.1	87.8	10.8	101.2	0.8	0.1	15.2	9.6	2.5
30.95	1.62	2.57	7.83	0.07	3.16	2.32	0.48	114.1	109.4	644.4	5.60	23.0	105.7	16.1	82.8	8.1	101.0	1.6	0.1	15.5	9.2	2.6
32.95	1.57	2.59	7.75	0.09	3.12	2.60	0.46	126.5	125.0	762.8	5.46	24.8	117.8	16.1	94.5	6.4	114.0	1.0	0.0	14.7	8.6	2.4
34.25	1.50	2.41	7.55	0.09	3.06	3.28	0.48	119.0	112.9	773.7	5.22	23.3	114.3	16.1	86.6	10.1	108.7	1.1	0.1	14.6	7.7	2.1

Table S-3 (Cont.)

position [m]	Na [%]	Mg [%]	Al [%]	P [%]	K [%]	Ca [%]	Ti [%]	V [ppm]	Cr [ppm]	Mn [ppm]	Fe [%]	Co [ppm]	Ni [ppm]	Cu [ppm]	Zn [ppm]	As [ppm]	Sr [ppm]	Mo [ppm]	Cd [ppm]	Pb [ppm]	Th [ppm]	U [ppm]
basement gneiss:																						
G1	2.96	0.16	7.25	0.00	5.03	0.37	0.07	9.3	3.7	119.9	0.28	2.1	7.5	15.1	17.7	-0.3	269.8	0.5	0.0	10.9	1.5	0.7
G2	5.85	0.11	7.36	0.02	1.32	0.85	0.04	9.8	7.4	94.7	0.21	2.1	2.4	4.3	7.3	-0.9	252.1	0.2	0.0	9.7	3.8	0.6
G3	4.45	0.12	7.18	0.03	2.64	1.35	0.07	8.2	2.2	156.4	0.40	1.8	3.6	0.7	11.0	-1.0	475.3	0.2	0.0	6.1	1.5	0.2
basement amphibolite:																						
A1	0.66	5.27	7.84	0.03	0.28	7.19	0.48	286.5	231.7	1856.3	10.23	49.3	77.3	71.6	78.6	-0.4	78.8	0.6	0.1	3.9	0.6	0.1
A2	1.41	3.28	7.56	0.08	0.36	6.46	0.78	283.3	195.5	1614.9	10.18	40.4	99.0	69.7	94.9	-0.8	165.8	0.4	0.0	2.1	1.3	0.3
A3	1.82	2.95	7.27	0.03	0.51	5.29	0.47	238.0	212.0	1266.9	7.26	31.5	82.3	46.5	93.0	-0.5	305.0	0.3	0.1	4.5	0.2	0.0
A4	3.75	1.75	8.32	0.12	0.68	3.71	0.42	106.1	78.2	623.4	4.13	19.5	65.1	59.2	61.4	0.5	505.1	0.2	-0.0	5.4	0.6	0.1
A5	1.58	6.60	6.44	0.03	0.43	5.88	0.33	138.3	1252.2	1669.8	8.40	41.4	264.8	6.0	113.9	-0.5	284.3	0.1	0.2	3.0	0.3	0.2
A6	1.64	5.19	7.19	0.13	0.44	6.32	0.60	245.9	330.4	1596.7	9.29	45.2	95.9	47.8	111.5	0.3	471.7	0.2	0.2	7.5	2.0	0.2
additional Stac Fada sample from different locality:																						
SF	2.36	2.38	7.26	0.07	1.98	1.14	0.43	91.7	221.3	765.5	4.39	31.3	382.8	26.7	110.0	0.7	270.2	0.2	0.0	7.4	4.4	0.9

1.5 Iron speciation

Iron speciation (Table S-4, Figs. 1, 3a) was done at UC Riverside, using established methods that sequentially extract carbonate-bound iron, ferric oxides and magnetite (Poulton and Canfield, 2005; Reinhard *et al.*, 2009; Reinhard *et al.*, 2013a). Approximately 100 mg of powder were weighed into 15 ml Falcon centrifuge tubes. The carbonate-bound fraction was extracted with 10ml of Na acetate buffered to pH 4.5 with acetic acid. The tubes were placed on a horizontal shaker table for 48 hours at room temperature. 5 ml of the solution were extracted with a pipette after centrifugation; the rest was discarded. The residual rock powder was then treated with Na dithionite (pH 4.8 for 2 hours) to dissolve the ferric oxide fraction and finally with NH_4-oxalate (pH 3.2 for 6 hours) to dissolve magnetite. The extracted solutions were diluted 1:100 with 2 % (v/v) HNO_3 and analysed by ICP-MS (Agilent 7500ce). The average reproducibility for iron concentrations in each fraction was 5 %, as determined by sample replicates.

The concentration of Ca and Ca/Mg ratios measured in the acetic acid fraction were used as an additional constraint on the abundance of carbonate in the samples. Assuming a $CaCO_3$ mineralogy, the obtained values agreed within 5 % (RE) on average with the carbonate abundance determined from the CO_2 pressure after phosphoric acid dissolution (see above). Carbonate concentrations plotted in Figure 1 are taken from the phosphoric acid treatment, except in cases where $\delta^{13}C_{carb}$ and $\delta^{18}O_{carb}$ were not measured (Table S-2).

Sulphide-bound iron was quantified by chromium reduction with Zn-acetate traps, followed by iodometric titration (Canfield *et al.*, 1986). Reproducibility was 4 % for sulphide-rich samples (>0.5 % chromium-reducible sulphur) and 20 % for sulphide-poor samples. To convert from the measured concentration of sulphide in the Zn-acetate traps to iron, we assumed a pyrite stoichiometry of FeS_2. To test for the relative importance of other metal sulphides such as pyrrhotite or sphalerite we processed a subset of samples with just concentrated boiling HCl, *i.e.* without the addition of $CrCl_2$ to the reaction vessels (Reinhard *et al.*, 2013a). The results showed that only up to 7 % (average 4 %) of the sulphide minerals in these samples are in this acid-volatile sulphide (AVS) phase, which is negligible in the summation of iron species in the bulk rock.

Table S-4 Iron speciation. Fe_{Carb} = carbonate-bound iron, Fe_{Ox} = ferric oxide-bound iron, Fe_{Mag} = magnetite-bound iron, Fe_{Py} = pyrite-bound iron. Fe_{HR} = highly reactive iron, which is the sum of all four phases. Fe_T = total iron from Table S-5. Fe_{Py} was not determined in most of the red shale facies and assumed to be zero as in the few examples. * = Carbonate content was calculated from the concentration of Ca in the acetic acid extract, assuming a $CaCO_3$ stoichiometry. Note that this calculation is an upper estimate, because it does not account for partial dissolution of silicates, which may become important below a carbonate content of 5 %, as suggested by the low molar Ca/Mg ratios in those samples.

position [m]	Fe_{Carb} [%]	Fe_{Ox} [%]	Fe_{Mag} [%]	Fe_{Py} [%]	Fe_{HR} [%]	Fe_{Py}/Fe_{HR} [by mass]	Fe_{HR}/Fe_T [by mass]	carb.* [%]	molar Ca/Mg
0	0.09	0.69	0.39		1.17	0.00	0.22	0.1	0.2
0.5	0.32	1.11	0.33		1.75	0.00	0.44	0.4	0.2
0.75	0.09	0.47	0.26		0.82	0.00	0.21	3.0	6.4
1.65	0.13	0.58	0.11		0.83	0.00	0.24	4.1	5.8

Table S-4 (Cont.)

position [m]	Fe$_{Carb}$ [%]	Fe$_{Ox}$ [%]	Fe$_{Mag}$ [%]	Fe$_{Py}$ [%]	Fe$_{HR}$ [%]	Fe$_{Py}$/Fe$_{HR}$ [by mass]	Fe$_{HR}$/Fe$_{T}$ [by mass]	carb.* [%]	molar Ca/Mg
2.05	0.07	0.60	0.34		1.02	0.00	0.19	2.3	7.3
2.73	0.59	0.51	0.21		1.31	0.00	0.36	11.8	4.3
2.77	0.16	0.32	0.11	0.00	0.60	0.00	0.21	18.2	28.3
2.8	0.10	0.35	0.18		0.64	0.00	0.11	0.5	1.2
2.83	0.17	0.47	0.14		0.78	0.00	0.20	14.7	23.2
2.87	0.17	0.27	0.13	0.00	0.58	0.00	0.18	17.4	28.3
3.2	0.76	0.68	0.38		1.81	0.00	0.35	1.9	0.7
3.7	0.29	0.16	0.19	0.00	0.64	0.00	0.14	1.9	2.4
4.1	0.10	0.53	0.18		0.81	0.00	0.30	20.6	49.0
4.38	0.11	0.45	0.11		0.67	0.00	0.23	26.9	64.0
4.42	0.10	0.27	0.09	0.01	0.47	0.03	0.22	31.1	76.4
4.65	0.49	0.17	0.23	0.07	0.95	0.07	0.26	5.3	2.9
4.75	0.16	0.07	0.10	1.23	1.57	0.78	0.37	10.0	21.3
4.9	0.23	0.08	0.11	1.15	1.58	0.73	0.36	15.8	28.0
5.3	0.13	0.08	0.08	0.27	0.56	0.48	0.17	19.3	46.6
5.45	0.19	0.20	0.22	1.36	1.98	0.69	0.44	19.3	8.8
5.6	0.27	0.56	0.23	0.00	1.06	0.00	0.24	14.2	23.4
5.65	0.79	0.07	0.12	1.11	2.09	0.53	0.49	15.2	17.7
5.8	0.12	0.07	0.08	0.24	0.51	0.46	0.15	11.7	23.5
6.5	0.37	0.16	0.24	0.00	0.77	0.00	0.19	9.8	5.9
7.1	0.18	0.38	0.17		0.73	0.00	0.18	12.6	21.7
12.1	0.03	1.55	0.32		1.89	0.00	0.32	1.5	3.5
13.05	0.02	1.33	0.24		1.60	0.00	0.25	4.8	14.0
14.65	0.02	0.99	0.30		1.31	0.00	0.23	5.6	15.8
16.05	0.03	1.14	0.25		1.42	0.00	0.26	7.3	14.3
16.85	0.04	1.27	0.26		1.57	0.00	0.29	7.4	12.3
20.45	0.02	0.83	0.26		1.11	0.00	0.20	6.1	15.6
22.75	0.02	0.98	0.28		1.28	0.00	0.24	7.8	17.5
24.55	0.02	1.05	0.33		1.40	0.00	0.28	9.2	20.0
25.75	0.02	0.95	0.25		1.22	0.00	0.23	6.5	19.0
25.95	0.03	1.00	0.26		1.29	0.00	0.24	8.2	24.7
27.55	0.03	1.09	0.28		1.40	0.00	0.30	6.8	13.9
29.15	0.03	1.03	0.27		1.32	0.00	0.26	6.3	18.7
30.95	0.02	1.18	0.29		1.49	0.00	0.27	5.2	14.0
32.95	0.02	0.88	0.26		1.16	0.00	0.21	5.8	17.6
34.25	0.01	0.84	0.22		1.08	0.00	0.21	7.4	22.4
42.1	0.01	1.79	0.31		2.11	0.00	0.32	0.2	0.5

1.6 Molybdenum isotope measurements

Molybdenum and strontium isotope measurements were performed at the Metal Geochemistry Center at Yale University, New Haven Connecticut. For molybdenum, an aliquot of the bulk digests prepared at UC Riverside split was doped with a Mo double spike. Using the known Mo concentrations (Table S-3), the spike was adjusted to maintain a constant sample to spike ratio. The mixture was evaporated at 100 °C, re-dissolved in 7 M HCl, and then purified by chromatographic separation. The ^{97}Mo-^{100}Mo double spike solution was prepared gravimetrically from Oak Ridge Laboratory metal powders as previously described (Asael *et al.*, 2013). A two-stage column procedure was applied for Mo purification, following standard protocols (Asael *et al.*, 2013; Planavsky *et al.*, 2014): The sample was run through an anion resin (AG-MP-1M) to separate Mo and Fe from the matrix followed by purification through a cation resin (AG50W-X8) to separate Mo from any remaining Fe. The Mo isotopic ratios were analysed using a Thermo Neptune Multi collector MC-ICP-MS instrument.

Molybdenum isotope compositions are reported using the δ notation, where $\delta^{98/95}$Mo (‰) = 1000 · [(^{98}Mo/^{95}Mo)$_{sample}$/(^{98}Mo/^{95}Mo)$_{NIST*99975}$ - 1], calculated relative to NIST 3134 (Lot 130418) with a value of +0.25 ‰ (Nägler *et al.*, 2014). A Calibration of the NIST standard relative to Rochester (Lot 862309E) gave: δ^{98}Mo$_{ROCH}$ = δ^{98}Mo$_{NIST3137}$ − 0.32 ± 0.12 ‰. For each sample, the target Mo concentration was 50 ppb during each session. In all reported samples the 1SD was <0.05 ‰. Duplicates (n = 6) of reference standard NOD-1 had an average δ^{98}Mo value of -0.41 ‰ and a standard deviation (SD) of 0.06 ‰. For SCo-1, for which there is to our knowledge no published reference value, we obtained a value of -0.07 ± 0.01 ‰ (1SD, n = 3). Values for Mo isotope measurements and associated errors can be found in Table S-5.

Table S-5 Molybdenum isotopes of bulk rocks, relative to NIST3134 = +0.25 ‰. Samples with reported standard deviations (SD) were prepared and analysed in replicates.

position [m]	$\delta^{98/95}$Mo [‰]	SD [‰]
–5.00	1.24	
–4.50	1.05	
0.00	1.00	
1.65	1.00	
2.73	0.35	
2.77	0.33	
2.80	0.52	
2.83	-0.31	0.02
3.20	0.30	
3.70	0.20	0.04
4.10	0.91	0.04
4.38	0.47	
4.42	0.30	

Table S-5 (Cont.)

position [m]	$\delta^{98/95}$Mo [‰]	SD [‰]
4.65	0.57	0.01
4.75	0.13	0.02
4.90	0.33	0.09
5.30	1.10	0.22
5.45	0.76	0.02
5.60	1.32	
5.65	1.19	0.01
5.80	0.68	0.03
6.50	0.43	
7.10	0.46	
12.10	-0.05	
13.05	-0.17	0.05
14.65	-0.16	
16.05	-0.34	0.02
16.85	-0.24	
20.45	-0.34	
22.75	-0.38	
24.55	-0.26	
25.75	-0.32	
25.95	-0.24	
29.15	-0.24	
30.95	-0.36	0.04
32.95	-0.34	
34.25	0.03	

1.7 Carbonate-bound strontium isotopes

Strontium was extracted from carbonate rocks following the sequential leaching protocol described by Bellefroid *et al.* (2015) (Table S-6), similar to that of Liu *et al.* (2013). Powdered samples were first washed with ammonium acetate to liberate any loosely bound Sr from clay surfaces. Around 400–500 mg of powder were weighed into 15 ml Falcon centrifuge tubes, mixed with 10 ml of 1M NH_4-acetate and left to react for 30 minutes at room temperature in an ultra-sonic bath. Solutions were centrifuged for 5 minutes at 5000 rpm, and then extracted with a pipette and transferred into a 15 ml screw-top Teflon beaker. Carbonate was then extracted from the same powder aliquot with acetic acid in eight steps with increasing acid strength. Acid quantities and concentrations are listed in Table S-6. Especially with the weakest acid, the solutions were carbonate-buffered, thus limiting the mobilisation of silicate-bound Sr. The silicate-bound

fraction was monitored with Rb/Sr ratios, which go up with increasing silicate dissolution. The clean carbonate end-member then corresponds to the extrapolated Rb/Sr ratio of 0.

The solid sample residues after acid treatment were dried at 80 °C for several days and weighed to calculate the cumulative extraction yield, which was on average 103 ± 11 % relative to the known carbonate content. Extracted solutions were evaporated at 80–100 °C overnight. They were then dissolved in weak nitric acid (5 % HNO_3 v/v), and 1000-fold dilution splits were measured for major and trace element abundances on a Thermo Element XR ICP-MS at the Yale Metal Geochemistry Center (Table S-7). A second split was taken from each solution and purified for ^{87}Sr/^{86}Sr analysis using an ESI PrepFast-MC-Sr system (Romaniello *et al.*, 2015). Samples were run on a Thermo Neptune MC-ICP-MS with NIST SRM 987 as a bracketing standard (average ^{87}Sr/^{86}Sr ratio of 0.71034 +/- 0.000062, 2SD). A subset of samples of the Lewisian basement and Stac Fada Mbr were analysed after bulk digestion without sequential leaching (Table S-8). The ^{87}Sr/^{86}Sr ratio at 1.2 billion years ago was calculated as $(^{87}$Sr/^{86}Sr$)_{1.2Ga} = (^{87}$Sr/^{86}Sr$)_{measured} - (^{87}$Rb/^{86}Sr$)_{modern} \cdot (e^{(\lambda \cdot t)} - 1)$, where λ is the decay constant ($1.42 \cdot 10^{-11}$ yr^{-1}) and $t = 1.2 \cdot 10^9$ years. The modern ^{87}Rb/^{86}Sr ratio was calculated from elemental concentrations, assuming relative abundances of 27.8 % for ^{87}Rb and 9.86 % for ^{86}Sr. Results are reported in Tables S-7 and S-8. One carbonate sample was processed in duplicate and the calculated carbonate end-member showed a standard deviation of 0.001. Analytical accuracy was assessed with the USGS carbonatite standard COQ-1, for which we obtained values of 0.70336 ± 0.000005, in good agreement with the value of 0.70331 ± 0.00002 (2SD) reported by Grünenfelder *et al.* (1986) for rocks from the same geologic unit. When COQ-1 was processed through the sequential extraction protocol, we obtained an average value of 0.70340 ± 0.00002 (2SD) for all acetic acid steps.

Table S-6 Dissolution method for carbonate bound Sr analysis.

Step	Reagent	Volume [ml]	Concentration [M]	pH
1-2	Ammonium Acetate	10	1	–
3-6	Acetic Acid	7.5	0.04	3.07
7-8	Acetic Acid	8	0.175	2.76
9	Acetic Acid	6	0.875	2.41
10	Acetic Acid	6	1.75	2.26

Table S-7 Elemental abundances and Sr isotopes of carbonate leaches. N1-N2 = ammonium acetate washing steps, S1-S8 = acetic acid extractions with increasing acid strength. Concentrations are relative to bulk rock.

sample	Mg [ppm]	Al [ppm]	Ca [%]	Mn [ppm]	Fe [ppm]	Rb [ppb]	Sr [ppb]	Rb/Sr	Mn/Sr	$^{87}Sr/^{86}Sr$
+4.20 m, N1	254	5	1.79	72	1	6044	31314	0.19	2.3	0.71553
+4.20 m, N2	103	4	1.59	115	1	523	21858	0.02	5.3	0.71272
+4.20 m, S1	116	2	3.80	346	0	185	21693	0.01	15.9	0.71072
+4.20 m, S2	118	2	4.39	410	1	201	23939	0.01	17.1	n.d.
+4.20 m, S3	93	36	2.29	218	4	127	13855	0.01	15.7	0.71061
+4.20 m, S4	108	126	0.63	78	8	135	7814	0.02	9.9	0.71303
+4.20 m, S5	145	461	0.39	49	23	144	5007	0.03	9.9	0.71562
+4.20 m, S6	169	441	0.14	21	34	142	2514	0.06	8.5	n.d.
+4.20 m, S7	222	656	0.11	19	85	104	1458	0.07	13.3	0.72046
+4.20 m, S8	219	626	0.12	17	76	102	1306	0.08	13.3	0.72028
+4.38 m, N1	194	6	1.59	55	1	1645	26980	0.06	2.1	0.72807
+4.38 m, N2	103	14	1.58	93	2	207	20878	0.01	4.4	0.71223
+4.38 m, S1	105	2	3.79	225	0	74	22782	0.00	9.9	0.70989
+4.38 m, S2	104	4	3.99	238	1	85	24011	0.00	9.9	0.70977
+4.38 m, S3	102	5	3.97	239	2	66	24744	0.00	9.6	0.70964
+4.38 m, S4	93	33	2.53	172	4	61	18276	0.00	9.4	0.71005
+4.38 m, S5	100	183	1.10	84	15	63	10218	0.01	8.2	0.71061
+4.38 m, S6	127	200	0.36	32	20	59	4404	0.01	7.3	0.71258
+4.38 m, S7	251	507	0.51	46	84	68	4864	0.01	9.4	0.71242
+4.38 m, S8	205	333	0.36	32	63	54	3121	0.02	10.2	0.71223
+4.90 m, N1	273	17	1.48	65	2	3129	31046	0.10	2.1	0.71398
+4.90 m, N2	124	28	1.35	100	5	317	28622	0.01	3.5	0.71156
+4.90 m, S1	115	7	2.91	215	1	117	25023	0.00	8.6	0.70999
+4.90 m, S2	157	22	3.08	234	3	192	29003	0.01	8.1	0.71004
+4.90 m, S3	161	140	0.65	78	10	150	12266	0.01	6.3	n.d.
+4.90 m, S4	162	133	0.25	30	12	91	6737	0.01	4.5	n.d.
+4.90 m, S5	211	348	0.26	29	37	91	6147	0.01	4.7	n.d.
+4.90 m, S6	248	329	0.14	18	48	78	4910	0.02	3.7	n.d.
+4.90 m, S7	245	413	0.07	11	88	54	1697	0.03	6.7	0.71635
+4.90 m, S8	351	659	0.10	15	135	63	1451	0.04	10.7	0.71751
+5.65 m, N1_rep1	546	15	1.66	64	2	5502	17301	0.32	3.7	0.72204
+5.65 m, N2_rep1	195	25	1.37	99	3	566	13203	0.04	7.5	0.71338
+5.65 m, S1_rep1	180	12	2.96	240	2	176	18463	0.01	13.0	0.71000
+5.65 m, S2_rep1	215	25	2.88	238	4	200	18912	0.01	12.6	0.71000
+5.65 m, S3_rep1	244	174	0.81	109	11	176	6244	0.03	17.5	0.71258
+5.65 m, S4_rep1	264	181	0.36	48	14	105	2869	0.04	16.6	0.7162

Table S-7 (Cont.)

sample	Mg [ppm]	Al [ppm]	Ca [%]	Mn [ppm]	Fe [ppm]	Rb [ppb]	Sr [ppb]	Rb/Sr	Mn/Sr	87Sr/86Sr
+5.65 m, S5_rep1	337	684	0.32	42	59	120	2419	0.05	17.2	0.72024
+5.65 m, S6_rep1	304	431	0.11	19	51	81	824	0.10	22.7	0.72909
+5.65 m, S7_rep1	644	1275	0.09	23	214	88	694	0.13	33.9	0.73967
+5.65 m, S8_rep1	561	1200	0.08	19	179	78	564	0.14	33.4	
+5.65 m, N1_rep2	533	9	1.25	51	1	5407	16337	0.33	3.1	0.72299
+5.65 m, N2_rep2	226	12	1.28	82	2	709	13812	0.05	5.9	0.71374
+5.65 m, S1_rep2	189	12	2.99	220	1	176	18944	0.01	11.6	0.70964
+5.65 m, S2_rep2	210	14	3.04	230	2	179	18929	0.01	12.2	0.70977
+5.65 m, S3_rep2	189	79	1.24	132	5	124	10000	0.01	13.2	0.71075
+5.65 m, S4_rep2	257	171	0.54	69	11	118	4531	0.03	15.3	0.71359
+5.65 m, S5_rep2	427	773	0.41	58	58	147	3335	0.04	17.4	0.71779
+5.65 m, S6_rep2	327	540	0.15	24	50	98	1156	0.08	21.0	0.72447
+5.65 m, S7_rep2	704	1512	0.15	31	210	97	1104	0.09	28.0	0.72969
+5.65 m, S8_rep2	527	1057	0.09	19	153	74	615	0.12	31.0	0.73106

Table S-8 Strontium isotope results of basement rocks and impact/volcanic debris layer. 87Sr/86Sr ratios at 1.2 Ga were calculated as described in Section S1.7.

ID	Sr [ppm]	Rb [ppm]	$(^{87}Sr/^{86}Sr)_{measured}$	$(^{87}Sr/^{86}Sr)_{1.2Ga}$	type
A6	579.3	7.9	0.70294	0.70227	mafic
A2	249.8	9.2	0.70689	0.70508	mafic
G2	242.1	23.8	0.72037	0.71554	felsic
G1	121.1	56.0	0.74991	0.72717	felsic
-5 m	198.5	46.7	0.71822	0.70666	impact/volcanic
-4.5 m	243.5	40.5	0.71422	0.70604	impact/volcanic

S2. Preservation of Primary Signatures

2.1 Alteration of Sr isotopes

It has been demonstrated in previous studies that Sr isotopic ratios of carbonates can be altered by later fluid infiltration into the host rock (Banner and Hanson, 1990). This form of alteration can also lead to a covariance between $\delta^{18}O_{carb}$ and $\delta^{13}C_{carb}$ and a lowering of absolute $\delta^{18}O_{carb}$ and $\delta^{13}C_{carb}$ values (Shields and Veizer, 2002; Bartley and Kah, 2004). Furthermore, anoxic diagenetic fluids can be enriched in Mn, thus leading to elevated Mn/Sr ratios (Gilleaudeau and Kah, 2013a). Our samples do indeed show a covariation between $\delta^{18}O_{carb}$ and

$\delta^{13}C_{carb}$, which may reflect some degree of fluid alteration of these rocks. We note, however, that such trends may also have been induced by primary environmental factors such as synchronous evaporation and oxidation of biomass. Mn/Sr ratios in carbonate extracts of our samples (range 3.7–33.9, average 12.4) overlap well with those of unaltered carbonates from the nearly contemporaneous (1.1 Ga) Taoudeni Basin in northwestern Africa (0.7–15.8, average 6.2, in the Aguelt el Mabha and Tourist formations; Gilleaudeau and Kah, 2013a). Even though we cannot fully exclude alteration based on these parameters, the data do not necessarily indicate massive secondary overprint.

Sr isotope fractionation almost exclusively leads to more radiogenic $^{87}Sr/^{86}Sr$ (Banner and Hanson, 1990; Brand, 2004). There are a few rare exceptions which show non-radiogenic alteration, however these typically show large local abundance of non-radiogenic country rock surrounding the carbonate units (*e.g.,* Miller *et al.,* 2008). In any case, Stoer Group fluid alteration would most likely have elevated the primary $^{87}Sr/^{86}Sr$ ratios, because meteoric fluids draining the hinterland should have been buffered by the Lewisian basement (0.715–0.851, Lyon *et al.,* 1975, this study). Rare earth element patterns and zircon age distributions of the Stoer sediments match those of the Lewisian gneiss, confirming that there was probably no other significant sediment source (Stewart, 2002 and references therein) and hence probably no other rock type that imparted a significant control on the water chemistry. Mafic rocks (now amphibolites) make up a very small component of the basement. This felsic buffering effect is illustrated by the presence of diagenetic K-feldspar in the Stac Fada Member underneath the Poll a'Mhuilt Member (Parnell *et al.,* 2011). The K-feldspar is thought to have been the first mineral that precipitated in gas escape structures immediately after the

proposed impact event that shaped sediment deposition in the Stac Fada Member (Parnell *et al.*, 2011). This event precedes the deposition of the Poll a'Mhuilt Member and could in itself not have contributed to alteration of our samples. Nevertheless, the presence of the K-feldspar is an example of felsic buffering of fluids at regional scale. Although the Stac Fada Member contains mafic volcanic fragments, the diagenetic K-feldspar suggests that the composition of fluids was dominated by that of the largely felsic mineralogy of the Lewisian gneiss and the Stoer Group sandstone. It is therefore unlikely that the mafic components of the Stac Fada Member or other mafic rocks in the Lewisian basement imparted a significant control on the composition of secondary fluids.

2.2 Metamorphic alteration of redox proxies

The metamorphic grade of the Poll a'Mhuilt Member is below greenschist facies (Stewart, 2002) and thus well within the range of other sedimentary rocks that have been studied successfully with the same biogeochemical proxies (*e.g.,* Anbar *et al.*, 2007; Reinhard *et al.*, 2009; Kendall *et al.*, 2011; Gilleaudeau and Kah, 2013b). Metamorphic effects on the Fe redox proxy and on Mo enrichments or isotopes have so far not been investigated systematically, but they are unlikely to have caused the observed patterns. Poulton and Raiswell (2002) showed that sedimentary rocks back to the Cambrian with palaeontological evidence for oxic conditions tend to have slightly lower Fe_{HR}/Fe_T ratios compared to modern oxic marine muds. They interpreted this observation as evidence for post-depositional Fe^{3+} reduction to mobilise Fe^{2+} which could subsequently have been lost. Alternatively, or in addition, they speculated that some reactive iron phases may react to form clays and thus get incorporated into the unreactive siliciclastic phase, which would also lower the Fe_{HR}/Fe_T ratio. These processes could potentially also have occurred in the Stoer Group with the implication that our measured Fe_{HR}/Fe_T ratios may originally have been higher, making it more likely that deep waters in the Stoer setting were indeed anoxic as discussed in the main text. Metamorphic addition of Mo is also unlikely, because there is no plausible Mo-rich source rock in the area (see discussion in Section S2.3).

2.3 Metasomatic effects on sulphide phases and Mo isotopes

As mentioned above and noted by Parnell *et al.* (2010; 2014), the calcareous grey shale in the middle Poll a'Mhuilt Member not only contains pyrite but also minor amounts of other sulphide mineral phases, including chalcopyrite, galena, sphalerite and greenockite. This finding raises the question of whether secondary fluids could have added excess amounts of sulphur and transition metals to these rocks, thus mimicking a euxinic signature with high Mo enrichments. These particular sulphide minerals are part of the acid-volatile sulphide phase (AVS) (Rohwerder and Sand, 2007), but our own measurements of this AVS component revealed that it makes up only between 1.9 and 7.6 % of the total sulphide mineral load. It is thus relatively minor. We further note that Cu, Pb, Zn and Cd show no to weak enrichments in our bulk rock data, which further indicates that they are not

anomalously abundant. Furthermore, the sulphide minerals occur as clusters and nodules that appear to be pre-compactional, because depositional laminae are deflected around them (Parnell *et al.*, 2010, 2014, this study). Sulphide laminae or veins are absent. This morphology points to an early diagenetic origin of the sulphide clusters and is inconsistent with precipitation from a late-stage fluid. It is further unlikely that such fluids, if they existed, were the source of the molybdenum, because much of the molybdenum is organic-bound as shown by XRF element maps presented by Parnell *et al.* (2015). We performed SEM analyses of the sulphide clusters and did not find any Mo above detection limit (<0.1 %). In contrast, if all Mo were sulphide-bound, then a rock with 200 ppm Mo and 2 % pyrite should show around 1 % Mo in the pyrite grains.

Lastly, it is difficult to envision a metasomatic fluid that is so highly enriched in Mo and S but shows only weak enrichments in other elements. On the other hand, seawater could plausibly explain this pattern. We speculate that the seawater that flooded this setting during high-tide or sealevel high-stand would have been from the photic zone, which, as today, was depleted in Cr, Co and Ni due to biological consumption (Yuan-Hui, 1991). Depletions in Zn and Cd may have been less extreme prior to the expansion of eukaryotic consumers (Dupont *et al.*, 2010; Scott *et al.*, 2012), allowing for minor accumulation in the photic zone and small enrichments in our samples. Molybdenum and U behave conservatively today, and As and V are only mildly depleted in the photic zone (Yuan-Hui, 1991). It is probable that Mo, U, As, and V had lower average concentrations in the Mesoproterozoic ocean (Sahoo *et al.*, 2012; Partin *et al.*, 2013; Reinhard *et al.*, 2013b), but that possibility does not preclude moderate abundances in oxic surface waters (*e.g.,* Algeo and Lyons, 2006). Hence, the enrichment patterns in the Poll a'Mhuilt shales may be a product of elemental profiles in seawater at that time.

2.4 Modern oxidative weathering

As noted in Figure 1, we observed a weathered horizon within the calcareous grey shale package, and the sample from that horizon was depleted in pyrite and Mo relative to surrounding samples. We excluded it from the discussion. If outcrop weathering had affected our samples at a larger scale, it would have weakened the primary signature that forms the basis of our interpretation. Modern weathering tends to preferentially mobilise isotopically heavy Mo (Pearce *et al.*, 2010), rendering the residue lighter. The isotopic enrichments of our grey shale samples relative to average crust thus cannot be explained by weathering effects. Overall, the degree of weathering on most of our samples was probably minor, because otherwise this relatively large amount of pyrite would not have been preserved. Pyrite weathers rapidly under the modern atmosphere (Petsch *et al.*, 2000). Oxidative weathering would have lowered the Fe_{Py}/Fe_{HR} ratio as iron sulphide (Fe_{Py}) would have been converted into iron oxide (part of Fe_{HR}). The fact that we still see Fe_{Py}/Fe_{HR} ratios up to 0.8 is thus a strong indication that oxidative weathering has not erased primary signatures.

S3. Potential Caveats for the Iron Redox Proxy

It is important to recognise that the iron redox proxy applied in this study was developed and calibrated with fine-grained marine muds and shales from environments with relatively low sedimentation rates (Berner, 1970; Raiswell *et al.*, 1988; Canfield, 1989; Raiswell *et al.*, 1994; Poulton and Canfield, 2005). Under these conditions, sediments from oxic water columns consistently display Fe_{HR}/Fe_T ratios of <0.38, while anoxic environments are enriched in Fe_{HR}/Fe_T (Canfield *et al.*, 1996; Raiswell and Canfield, 1996, 1998; Raiswell *et al.*, 2001; Wijsman *et al.*, 2001; Lyons *et al.*, 2003). There are two possible sources of reactive iron that can lead to such enrichments: (1) hydrothermal vents on the seafloor, which may have been particularly important sources of iron in the Precambrian when the deep ocean was largely anoxic and dissolved Fe could stay in solution (*e.g.,* Isley and Abbott, 1999; Poulton and Raiswell, 2002; Poulton and Canfield, 2011) and (2) diagenetic mobilisation of iron from pore waters on the continental shelf, followed by redeposition in other parts of the basin ("iron shuttle", Canfield *et al.*, 1996; Lyons, 1997; Wijsman *et al.*, 2001). Hence, for the Fe_{HR}/Fe_T proxy to be applicable, two conditions have to be fulfilled. First, either one or both of these reactive iron sources have to be present and, second, sedimentation rates need to be sufficiently low such that accumulations of authigenic iron minerals are not diluted by siliciclastic background sedimentation (Lyons and Berner, 1992; Lyons and Severmann, 2006).

In the case of the Poll a'Mhuilt Member, sedimentation rates were probably not exceedingly high because in that case we should not expect to observe such marked enrichments in Mo. However, the first condition, a reactive iron source, may not have been fulfilled in this particular setting. As discussed above and in the main text, the Mo enrichment is most parsimoniously explained by influx of surface seawater, which was likely oxygenated in the mid-Proterozoic (Stüeken, 2013; Reinhard *et al.*, 2016; Hardisty *et al.*, 2017; Koehler *et al.*, 2017). Oxic waters do not carry significant amounts of dissolved iron because of the insolubility of the Fe^{3+} state. We can therefore rule out an external input of iron into the Stoer setting from the open ocean, including from hydrothermal vents. The burden thus lies on the intrabasinal iron shuttle. In this scenario, iron is mobilised from sediments by diagenetic reduction of Fe^{3+} to Fe^{2+}, which can then escape into the water column and get transported in the form of colloids or organic complexes (reviewed by Raiswell, 2011). The release requires suppressed sulphate reduction rates in pore waters, such that Fe^{2+} is not captured in sulphide minerals, and it is aided by bioturbation. Both factors may not have been applicable in the Stoer setting. Sulphate levels high enough to reach gypsum saturation may have fostered diagenetic sulphate reduction and Fe^{2+} retention. Furthermore, bioturbation would have been absent at 1.2 Ga, making it more difficult for Fe^{2+} to be released from pore waters into the water column. Lastly, rapid evaporation and desiccation of shallow sedimentary beds where diagenetic Fe^{3+} reduction may have taken place could further have impeded iron transport and enrichment of

Fe_{HR}/Fe_T in deeper sediments. Iron shuttling has so far not been investigated in evaporitic settings, but for these reasons listed above it may not operate as efficiently as it does in open marine systems.

In conclusion, our measured Fe_{HR}/Fe_T ratios likely provide a conservative estimate of the water column redox state. Although only two of the black shales samples fall firmly into the empirically defined anoxic field in Figure 3a ($Fe_{HR}/Fe_T > 0.38$), it is likely that the lower part of the water column was indeed anoxic, as supported by the high enrichments in Mo, which are highly uncharacteristic of oxic sediments (Scott and Lyons, 2012).

Supplementary Information References

ALGEO, T.J., LYONS, T.W. (2006) Mo–total organic carbon covariation in modern anoxic marine environments: Implications for analysis of paleoredox and paleohydrographic conditions. *Paleoceanography* 21, doi: 10.1029/2004PA001112.

ANBAR, A., DUAN, Y., LYONS, T.W., ARNOLD, G.L., KENDALL, B., CREASER, R.A., KAUFMAN, A.J., GORDON, G.W., SCOTT, C.T., GARVIN, J., BUICK, R. (2007) A whiff of oxygen before the Great Oxidation Event? *Science* 317, 1903–1906.

ASAEL, D., TISSOT, F.L., REINHARD, C.T., ROUXEL, O., DAUPHAS, N., LYONS, T.W., PONZEVERA, E., LIORZOU, C., CHÉRON, S. (2013) Coupled molybdenum, iron and uranium stable isotopes as oceanic paleoredox proxies during the Paleoproterozoic Shunga Event. *Chemical Geology* 362, 193–210.

BANNER, J.L., HANSON, G.N. (1990) Calculations of simultaneous isotopic and trace element variations during water-rock interaction with applications to carbonate diagenesis. *Geochimica et Cosmochimica Acta* 54.

BARTLEY, J.K., KAH, L.C. (2004) Marine carbon reservoir, C_{org}-C_{carb} coupling, and the evolution of the Proterozoic carbon cycle. *Geology* 32, 129–132.

BELLEFROID, E.J., PLANAVSKY, N., JIANG, G., HOOD, A. (2015) A Sequential Leaching Method to Measuring Primary Signatures on Partially Altered Bulk Carbonates. *Goldschmidt Conference 2015 (Prague)*, A248.

BERNER, R.A. (1970) Sedimentary pyrite formation. *American Journal of Science* 268, 1–23.

BRAND, U. (2004) Carbon, oxygen and strontium isotopes in Paleozoic carbonate components: an evaluation of original seawater-chemistry proxies. *Chemical Geology* 204, 23–44.

CANFIELD, D.E. (1989) Reactive iron in marine sediments. *Geochimica et Cosmochimica Acta* 53, 619–632.

CANFIELD, D.E., LYONS, T.W., RAISWELL, R. (1996) A model for iron deposition to euxinic Black Sea sediments. *American Journal of Science* 296, 818–834.

CANFIELD, D.E., RAISWELL, R., WESTRICH, J.T., REAVES, C.M., BERNER, R.A. (1986) The use of chromium reduction in the analysis of reduced inorganic sulphur in sediments and shales. *Chemical Geology* 54, 149–155.

DUPONT, C.L., BUTCHER, A., VALAS, R.E., BOURNE, P.E., CAETANO-ANOLLÉS, G. (2010) History of biological metal utilization inferred through phylogenomic analysis of protein structures. *Proceedings of the National Academy of Sciences* 107, 10567–10572.

GILLEAUDEAU, G.J., KAH, L.C. (2013a) Carbon isotope records in a Mesoproterozoic epicratonic sea: carbon cycling in a low-oxygen world. *Precambrian Research* 228, 85–101.

GILLEAUDEAU, G.J., KAH, L.C. (2013b) Oceanic molybdenum drawdown by epeiric sea expansion in the Mesoproterozoic. *Chemical Geology* 356, 21–37.

GRÜNENFELDER, M.H., TILTON, G.R., BELL, K., BLENKINSOP, J. (1986) Lead and strontium isotope relationships in the Oka carbonatite complex, Quebec. *Geochimica et Cosmochimica Acta* 50, 461–468.

HARDISTY, D.S., LU, Z., BEKKER, A., DIAMOND, C.W., GILL, B.C., JIANG, G., KAH, L.C., KNOLL, A.H., LOYD, S.J., OSBURN, M.R., PLANAVSKY, N.J. (2017) Perspectives on Proterozoic surface ocean redox from iodine contents in ancient and recent carbonate. *Earth and Planetary Science Letters* 463, 159–170.

ISLEY, A.E., ABBOTT, D.H. (1999) Plume-related mafic volcanism and the deposition of banded iron formation. *Journal of Geophysical Research: Solid Earth* 104, 15461–15477.

KENDALL, B., GORDON, G.W., POULTON, S.W., ANBAR, A.D. (2011) Molybdenum isotope constraints on the extent of late Paleoproterozoic ocean euxinia. *Earth and Planetary Science Letters* 307, 450–460.

KOEHLER, M.C., STÜEKEN, E.E., KIPP, M.A., BUICK, R., KNOLL, A.H. (2017) Spatial and temporal trends in Precambrian nitrogen cycling: a Mesoproterozoic offshore nitrate minimum. *Geochimica et Cosmochimica Acta* 198, 315–337.

LIU, C., WANG, Z., RAUB, T.D. (2013) Geochemical constraints on the origin of Marinoan cap dolostones from Nuccaleena Formation, South Australia. *Chemical Geology* 351, 95–104.

LYON, T.D.B., GILLEN, C., BOWES, D.R. (1975) Rb-Sr isotopic studies near the major Precambrian junction, between Scourie and Loch Laxford, northwest Scotland. *Scottish Journal of Geology* 11, 333–337.

LYONS, T.W. (1997) Sulphur isotopic trends and pathways of iron sulphide formation in upper Holocene sediments of the anoxic Black Sea. *Geochimica et Cosmochimica Acta* 61, 3367–3382.

LYONS, T.W., BERNER, R.A. (1992) Carbon-sulphur-iron systematics of the uppermost deep-water sediments of the Black Sea. *Chemical Geology* 99, 1–27.

LYONS, T.W., SEVERMANN, S. (2006) A critical look at iron paleoredox proxies: new insights from modern euxinic marine basins. *Geochimica et Cosmochimica Acta* 70, 5698–5722.

LYONS, T.W., WERNE, J.P., HOLLANDER, D.J., MURRAY, R.W. (2003) Contrasting sulphur geochemistry and Fe/Al and Mo/Al ratios across the last oxic-to-anoxic transition in the Cariaco Basin, Venezuela. *Chemical Geology* 195, 131–157.

MILLER, N., JOHNSON, P.R., STERN, R.J. (2008) Marine Versus Non-Marine Environments for the Jibalah Group, NW Arabian Shield:--A Sedimentologic and Geochemical Survey and Report of Possible Metazoa in the Dhaiqa Formation. *Arabian Journal for Science and Engineering* 33, 55–78.

NÄGLER, T.F., ANBAR, A.D., ARCHER, C., GOLDBERG, T., GORDON, G.W., GREBER, N.D., SIEBERT, C., SOHRIN, Y., VANCE, D. (2014) Proposal for an international molybdenum isotope measurement standard and data representation. *Geostandards and Geoanalytical Research* 38, 149–151.

PARNELL, J., BOYCE, A.J., MARK, D., BOWDEN, S., SPINKS, S. (2010) Early oxygenation of the terrestrial environment during the Mesoproterozoic. *Nature* 468, 290–293.

PARNELL, J., MARK, D., FALLICK, A.E., BOYCE, A., THACKREY, S. (2011) The age of the Mesoproterozoic Stoer Group sedimentary and impact deposits, NW Scotland. *Journal of the Geological Society* 168, 349–358.

PARNELL, J., STILL, J., SPINKS, S., THAYALAN, W., BOWDEN, S. (2014) Cadmium sulphide in a Mesoproterozoic terrestrial environment. *Mineralogical Magazine* 78, 47–54.

PARNELL, J., SPINKS, S., ANDREWS, S., THAYALAN, W., BOWDEN, S. (2015) High Molybdenum availability for evolution in a Mesoproterozoic lacustrine environment. *Nature Communications* 6, doi:10.1038/ncomms7996.

PARTIN, C.A., LALONDE, S.V., PLANAVSKY, N.J., BEKKER, A., ROUXEL, O.J., LYONS, T.W., KONHAUSER, K.O. (2013) Uranium in iron formations and the rise of atmospheric oxygen. *Chemical Geology* 362, 82–90.

PEARCE, C.R., BURTON, K.W., VON STRANDMANN, P.A.P., JAMES, R.H., GÍSLASON, S.R. (2010) Molybdenum isotope behaviour accompanying weathering and riverine transport in a basaltic terrain. *Earth and Planetary Science Letters* 295, 104–114.

PETSCH, S.T., BERNER, R.A., EGLINTON, T.I. (2000) A field study of the chemical weathering of ancient sedimentary organic matter. *Organic Geochemistry* 31, 475–487.

PLANAVSKY, N.J., ASAEL, D., HOFMANN, A., REINHARD, C.T., LALONDE, S.V., KNUDSEN, A., WANG, X., OSSA OSSA, F., PECOITS, E., SMITH, A.J.B., BEUKES, N.J., BEKKER, A., JOHNSON, T.M., KONHAUSER, K., LYONS, T.W., ROUXEL, O.J. (2014) Evidence for oxygenic photosynthesis half a billion years before the Great Oxidation Event. *Nature Geoscience* 7, 283–286.

POULTON, S.W., CANFIELD, D.E. (2005) Development of a sequential extraction procedure for iron: implications for iron partitioning in continentally derived particulates. *Chemical Geology* 214, 209–221.

POULTON, S.W., CANFIELD, D.E. (2011) Ferruginous conditions: a dominant feature of the ocean through Earth's history. *Elements* 7, 107–112.

POULTON, S.W., RAISWELL, R. (2002) The low-temperature geochemical cycle of iron: from continental fluxes to marine sediment deposition. *American Journal of Science* 302, 774–805.

RAISWELL, R. (2011) Iron transport from the continents to the open ocean: The aging–rejuvenation cycle. *Elements* 7, 101–106.

RAISWELL, R., CANFIELD, D.E. (1996) Rates of reaction between silicate iron and dissolved sulphide in Peru Margin sediments. *Geochimica et Cosmochimica Acta* 60, 2777–2787.

RAISWELL, R., CANFIELD, D.E. (1998) Sources of iron for pyrite formation in marine sediments. *American Journal of Science* 298, 219–245.

RAISWELL, R., BUCKLEY, F., BERNER, R.A., ANDERSON, T.F. (1988) Degree of pyritization of iron as a paleoenvironmental indicator of bottom-water oxygenation. *Journal of Sedimentary Research* 58, 812–819.

RAISWELL, R., CANFIELD, D.E., BERNER, R.A. (1994) A comparison of iron extraction methods for the determination of degree of pyritisation and the recognition of iron-limited pyrite formation. *Chemical Geology* 111, 101–110.

RAISWELL, R., NEWTON, R., WIGNALL, P.B. (2001) An indicator of water-column anoxia: resolution of biofacies variations in the Kimmeridge Clay (Upper Jurassic, UK). *Journal of Sedimentary Research* 71, 286–294.

REINHARD, C.T., RAISWELL, R., SCOTT, C.T., ANBAR, A., LYONS, T.W. (2009) A late Archaean sulfidic sea stimulated by early oxidative weathering of the continents. *Science* 326, 713–716.

REINHARD, C.T., LYONS, T.W., ROUXEL, O., ASAEL, D., DAUPHAS, N., KUMP, L.R. (2013a) Iron Speciation and Isotope Perspectives on Palaeoproterozoic Water Column Chemistry. In: Kump, L.R., Kuznetsov, A.B., Gorokhov, I.M., Melezhik, V.A., Farkaš, J., Chakrabarti, R., Jacobsen, S.B., Reinhard, C.T., Lyons, T.W., Rouxel, O., Asael, D., Dauphas, N., van Zuilen, M., Schoenberg, R., Tissot, F.L.H., Hannah, J.L., Stein, H.J. (Eds.) *Reading the Archive of Earth's Oxygenation.* Springer, Berlin, 1483–1492.

REINHARD, C.T., PLANAVSKY, N.J., ROBBINS, L.J., PARTIN, C.A., GILL, B.C., LALONDE, S.V., BEKKER, A., KONHAUSER, K.O., LYONS, T.W. (2013b) Proterozoic ocean redox and biogeochemical stasis. *Proceedings of the National Academy of Sciences,* 110, 5357–5362.

REINHARD, C.T., PLANAVSKY, N., OLSON, S.L., LYONS, T.W., ERWIN, D.H. (2016) Earth's oxygen cycle and the evolution of animal life. *Proceedings of the National Academy of Sciences,* doi: 10.1073/pnas.1521544113.

ROHWERDER, T., SAND, W. (2007) Mechanisms and biochemical fundamentals of bacterial metal sulphide oxidation. In: Donati, E.R., Sand, W. (Eds.) *Microbial processing of metal sulphides.* Springer Netherlands, Amsterdam, 35–58.

ROMANIELLO, S.J., FIELD, M.P., SMITH, H.B., GORDON, G.W., KIM, M.H., ANBAR, A.D. (2015) Fully automated chromatographic purification of Sr and Ca for isotopic analysis. *Journal of Analytical Atomic Spectrometry* 30, 1906–1912.

SAHOO, S.K., PLANAVSKY, N.J., KENDALL, B., WANG, X., SHI, X., SCOTT, C., ANBAR, A.D., LYONS, T.W., JIANG, G. (2012) Ocean oxygenation in the wake of the Marinoan glaciation. *Nature* 489, 546–549.

SCOTT, C., LYONS, T.W. (2012) Contrasting molybdenum cycling and isotopic properties in euxinic versus non-euxinic sediments and sedimentary rocks: refining the paleoproxies. *Chemical Geology* 324, 19–27.

SCOTT, C., PLANAVSKY, N.J., DUPONT, C.L., KENDALL, B., GILL, B.C., ROBBINS, L.J., HUSBAND, K.F., ARNOLD, G.L., WING, B., POULTON, S.W., BEKKER, A., ANBAR, A., KONHAUSER, K., LYONS, T.W. (2012) Bioavailability of zinc in marine systems through time. *Nature Geoscience* 6, 125–128.

SHIELDS, G., VEIZER, J. (2002) Precambrian marine carbonate isotope database: Version 1.1. *Geochemistry Geophysics Geosystems* 3, doi: 10.1029/2001GC000266.

STEWART, A.D. (2002) *The later Proterozoic Torridonian rocks of Scotland: Their sedimentology, geochemistry and origin.* Geological Society, Bath.

STÜEKEN, E.E. (2013) A test of the nitrogen-limitation hypothesis for retarded eukaryote radiation: nitrogen isotopes across a Mesoproterozoic basinal profile. *Geochimica et Cosmochimica Acta* 120, 121–139.

WIJSMAN, J.W., MIDDELBURG, J.J., HERMAN, P.M., BÖTTCHER, M.E., HEIP, C.H. (2001) Sulphur and iron speciation in surface sediments along the northwestern margin of the Black Sea. *Marine Chemistry* 74, 261–278.

YUAN-HUI, L. (1991) Distribution patterns of the elements in the ocean: A synthesis. *Geochimica et Cosmochimica Acta* 55, 3223–3240.